



## Article

# Sentinel-1 Response to Canopy Moisture in Mediterranean Forests before and after Fire Events

Francesco Pirotti <sup>1,2,\*</sup> , Opeyemi Adedipe <sup>1</sup> and Brigitte Leblon <sup>3</sup>

<sup>1</sup> Department of Land, Environment, Agriculture and Forestry (TESAF), University of Padua, Viale dell'Università 16, 35020 Legnaro, Italy

<sup>2</sup> Interdepartmental Research Center of Geomatics (CIRGEO), University of Padua, Viale dell'Università 16, 35020 Legnaro, Italy

<sup>3</sup> Faculty of Natural Resources Management, Lakehead University, Thunder Bay, ON BB 1001H, Canada

\* Correspondence: francesco.pirotti@unipd.it

**Abstract:** This study investigates the sensibility of Sentinel-1 C-band backscatter to the moisture content of tree canopies over an area of about 500 km<sup>2</sup> in north-western Portugal, with specific analysis over burnt areas. Sentinel-1 C-VV and C-VH backscatter values from 276 images acquired between January 2018 and December 2020 were assigned to five classes depending on the Drought Code (DC) scenario over several unburned and burned sites with total (>90%) forest canopy cover. Confounding variables such as tree cover and incidence angle were accounted for by masking using specific thresholds. The following results are discussed: (a) C-VV and C-VH backscatter values are inversely correlated ( $R^2 = 0.324$  to  $0.438 - p < 0.001$ ) with local incidence angle over canopies; (b) correlation is significantly stronger over very wet scenarios (DC class = 0 to 1); (c) C-VV and C-VH backscatter values can discriminate wet to dry forest environments, but they are less sensitive to the transition between dry (DC classes = 1 to 10, 10 to 100) and extremely dry environments (DC classes = 100 to 1000); (d) C-VH is more sensible than C-VV to capture burnt canopy; and (e) the C-VH polarization captures post-fire recovery after an average minimum period of 360 days after the fire event, although with less distinction for extremely wet soils. We conclude that C-band VH backscatter intensity decreases from wet to dry canopy conditions, that this behavior of the backscatter signal with respect to canopy dryness is lost after a fire event, and that after one year it is recovered.

**Keywords:** Drought Code; Sentinel-1; fire danger; tree cover; canopy moisture; radar



**Citation:** Pirotti, F.; Adedipe, O.; Leblon, B. Sentinel-1 Response to Canopy Moisture in Mediterranean Forests before and after Fire Events. *Remote Sens.* **2023**, *15*, 823. <https://doi.org/10.3390/rs15030823>

Academic Editors: Antonino Maltese, Mauro Lo Brutto and Gino Dardanelli

Received: 9 December 2022

Revised: 21 January 2023

Accepted: 30 January 2023

Published: 1 February 2023



**Copyright:** © 2023 by the authors. Licensee MDPI, Basel, Switzerland. This article is an open access article distributed under the terms and conditions of the Creative Commons Attribution (CC BY) license (<https://creativecommons.org/licenses/by/4.0/>).

## 1. Introduction

Forest fires are a significant disturbance affecting forest dynamics in several forested ecosystems, particularly in the Mediterranean regions. Mediterranean Europe has been highly susceptible to mega-fires due to drought and topography that promote fire ignition [1,2]. Italy, France, and Spain typically have numerous fire events, with more than 100,000 ha burned annually [3]. In the Mediterranean region, fire danger is monitored using the Canadian Forest Fire Danger Rating System (CFFDRS). One of its systems is the Fire Weather Index (FWI), comprising fuel moisture codes and fire behavior sub-indexes (Figure 1). The system estimates mid-afternoon fire danger based on weather variables (temperature, wind speed, and relative humidity) observed at noon and rainfall intensity measured over 24 h [4].

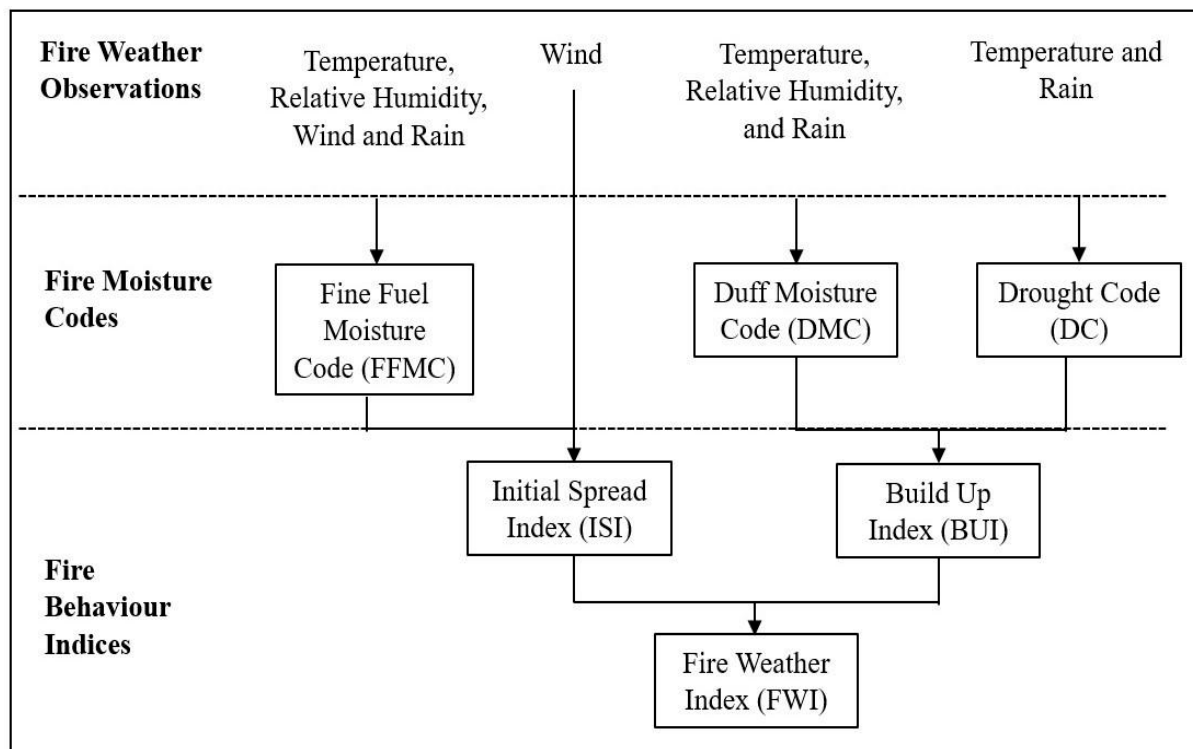


**Figure 1.** Structure of the Canadian Forest Fire Weather Index (adapted from [4]).

The FWI has several moisture codes. According to [5], the Fine Fuel Moisture Code (FFMC) is related to pine litter of 1.2 cm thickness and fuel weight of 0.25 kg/m<sup>2</sup>. The Duff Moisture Code (DMC) is the moisture of the top 7 cm of forest layers where decay occurs with a fuel load of 5 kg/m<sup>2</sup>. The (DC) is the moisture availability at 18 cm thickness of organic matter and fuel capacity of 25 kg/m<sup>2</sup>. These three codes are related to a different fuel that has a time-lag period or the time elapsed for two-thirds loss of soil moisture at 20 °C and 40% RH [4,6]. FFMC has a time lag of 2/3 day, DMC has a time lag of 12 days, and DC has a time lag of 52 days. Furthermore, the drying rate of each fuel type significantly depends on the previous day's code values [4]. Fuel behavior indices include the Initial Spread Index (ISI), the Buildup Index (BUI), and the Fire Weather Index (FWI). The CFFDRS was developed over data acquired over mature jack pine (*Pinus banksiana*) and lodgepole pine (*Pinus contorta*) forests, with the hypothesis that these two pine species have similar structural arrangements and fire dynamics as all other forests [5]. The CFFDRS FWI codes have been tested abroad. Yang and Di [7] evaluated the applicability of the CFFDRS to monitor fire dangers in North-Eastern China, where climatic conditions are similar to Canadian boreal forests. Strong correlations were also derived between the DC and the number of fire occurrences in a *Pinus halepensis* forest in the Greek Mediterranean region, where the forest types differ from the Canadian boreal forests [8].

However, the accuracy of mapping fire danger with FWI is limited to small geographical areas, mainly when meteorological observations are collected at sparse weather stations [9]. For the Mediterranean regions, the EU Joint Research Center (JRC) uses Numerical Weather Prediction (NWP) and High Resolution (HRES) models for interpolating between the weather station data. As shown in [10], the HRES model operates at a horizontal resolution of 16 km and provides accurate weather prediction for ten days upfront. Another limitation of FWI is its standard configuration for only two pine species [5], and thus it might not be accurate when applied to other forest types.

A suitable alternative is to use remote sensing techniques [11,12]. Among all the FWI codes, the Drought Code (DC) can be considered a reliable proxy in estimating fuel moisture. It is worth noting that DC is a useful indicator of seasonal drought effects on forest fuels [13]. Strong correlations were found between DC and optical data from the Advanced Very High-

Resolution Radiometer (AVHRR) of National Oceanic and Atmospheric Administration (NOAA) in Indonesia [14] and in Canadian boreal forests [9].

However, optical imagery has the drawback of limited availability to clear sky conditions. This is not the case with active SAR sensors that can acquire images, whatever the sky conditions. Synthetic Aperture Radar (SAR) sensors provide fine spatial resolution data and allow for 24-hour image acquisition, even in meteorological situations perturbing optical satellites' efficacy [15,16].

Radar imageries were shown to be very suitable in several fire studies. Cross-polarized (C-VH) backscatter is excellent for assessing the difference between bare land and forests, while the C-HH co-polarization is best for detecting the backscatter sensitivity to soil moisture after fire incidents [16,17]. DC values were shown to correlate well with SAR C-band backscatter extracted from RADARSAT-1 and ERS (1 and 2) imagery in northern boreal forests [6,18,19] and RADARSAT-2 polarimetric data [17]. However, according to [20], SAR beams are also sensitive to terrain roughness and biomass build-up.

Among all the new SAR sensors, Sentinel-1 has several advantages. It is a constellation system, i.e., two orbiting platforms (Sentinel-1A and -1B) that allow image acquisition at 10 m resolution with a 6-day repeat cycle in horizontal and vertical polarization modes (VV and VH) [21]. Sentinel-1 C-VV and C-VH backscatter variations were linked to meteorological events, forest floor moisture, and canopy moisture in a deciduous forest in France [22]. Sentinel-1 C-VV imagery was used to estimate soil moisture in open sites in India [23] and over a mixed forest in the United States [24].

The main objective of this study is to assess the capability of Sentinel-1 C-band vertical-vertical (C-VV) and vertical-horizontal (C-VH) polarization radar backscatter signal in delineating moisture regimes, as defined by DC values in north-western Portugal. As a secondary objective, differences in the sensitivity of C-VV and C-VH backscatters for mapping pre-fire and post-fire moisture conditions will also be assessed. Both variables (backscatter and DC) were acquired from the 2018–2020 time series. The analysis will be only done for sites with substantial tree cover to reduce the tree cover's effects. In the study, we will also consider the effect of the local incidence angle on the radar backscatter. In particular, the analysis will be performed in three types of areas: (a) unburnt areas, (b) burnt areas before the fire (pre-fire), and (c) burnt areas after the fire (post-fire). The relationship between backscatter values and DC classes as a function of the Local Incidence Angle (LIA) will be investigated with linear regression models. Corrected backscatter values will be analyzed with box plots as a function of DC classes, satellite, and polarization.

The main points of interest of the current work are related to better understanding the behavior of backscatter of C-band SAR with respect to canopies in different moisture conditions, from drought to wet canopies, and what happens when fire events change the canopy structure. We discuss results that show that wet canopies consistently provide a stronger backscatter than dry canopies. We show that canopies after fire events lose this type of response, likely due to the fire changing the composition of the canopy in terms of the ratio between leaves, and small and larger branches.

## 2. Materials and Methods

### 2.1. Study Area

The study area of 502.42 km<sup>2</sup> is located in the municipalities of Viana do Castelo and Braga in north-western Portugal (41–42° North Latitude, 8–9° West Longitude) (Figure 2). The area elevation ranges from 0 m above sea level (ASL) in the vicinity of Viana do Castelo and Braga to 1500 m ASL at the bordering regions of Melgaço and Cabeceiras de Basto (Figure 3). From the vegetation point of view, the study area includes broadleaf and conifer tree species, mainly the maritime pine (*Pinus pinaster*) and eucalyptus (*Eucalyptus globulus*) [25]. According to the Köppen–Geiger climate classification [26], both municipalities are classified as CSB, meaning a warm temperate climate with dry and warm summers. Between 1981 and 2010, the mean daily temperatures were the highest in August in Viana do Castelo (20.8 °C) and Braga (21.4 °C) [27]. Over the same period, the mean precipitations

were 38.5 mm (Viana do Castelo) and 21.4 mm (Braga). Such climatic conditions are related to high land surface dryness and, thus, the susceptibility to fire incidences [28]. The EU Joint Research Centre (JRC) reported that 70% of fire incidents in 2020 in Portugal occurred in July, August, and September [29]. In 2006, fire events affected 15,706 ha in Viana do Castelo and 10,265 ha in Braga [30].

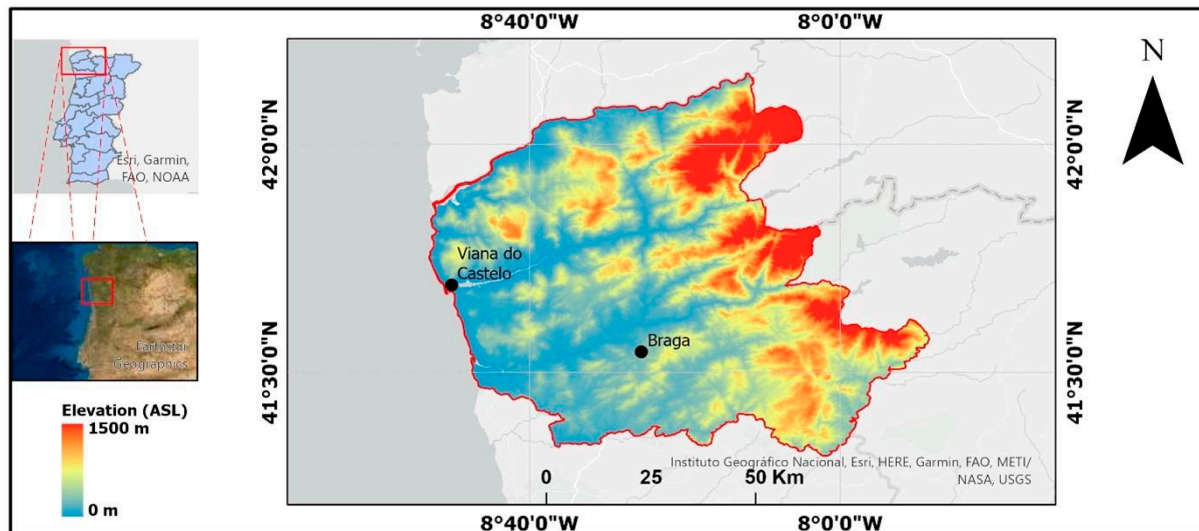


**Figure 2.** Location of the study area and the corresponding digital elevation model (DEM).

## 2.2. SAR Imagery

This study used SAR imagery acquired by the European Space Agency (ESA) Sentinel-1 (S1) satellite, with the TOPSAR (Terrain Observation with a Progressive Scanning SAR) sensor. Sentinel-1 consists of a constellation of two satellites, A and B, each having a sensor that operates in the C-band with a central frequency of 5.405 GHz and a wavelength of 5.6 cm [31]. The first Sentinel-1 platform was launched in April 2016. With a swath width of 250 km, it provides a return time of about six days. A total of 276 scenes covering the study area were downloaded from SciHub Copernicus Hub, covering 181 days over the three years (2018, 2019, and 2020) that are considered in this study. The image data consisted of Level-1 Ground Range Detected (GRD) types in the high-resolution Interferometric Wide (IW) swath mode. The scenes were from the same ascending orbit (147), thus having the same incidence angles between 30.42 and 46.03° from one date to another. Furthermore, local incidence angles ranging from 2.07 to 64.72° were constant from one date to another, as the area's topography does not change with time.

## 2.3. Fire Maps

Because the study aims to analyze the connection between DC values and C-band backscatter values before and after fire events, we identified fire areas in the analysis. They were extracted from the European Forest Fire Information System (EFFIS) [32]. The maps provide the areas that were subjected to fire disturbance over the three-year study period. The fire areas range from 2 ha to 675 ha. Vegetation in these fire-affected areas includes broad leaves and conifers. According to [32], EFFIS uses the Rapid Damage Assessment (RDA) technique to map fire events. The RDA involves the use of AQUA and TERRA satellites of the Moderate Resolution Imaging Spectroradiometer (MODIS) sensor to map > 30 ha fire events, and Sentinel-2 imagery to map fire events < 30 ha.

## 2.4. Tree Cover Map

As shown in [17], the relationship between SAR backscatter and DC values highly depends on the tree cover. In particular, the relationship between SAR backscatters and DC values differs for burned and unburned areas. In addition, recovery mechanisms

from fires in Mediterranean forests depend on the tree cover [33]. Therefore, the study only considered unburnt and burnt (pre-fire periods) sites that are completely covered by tree canopies. To define such sites, we used tree cover data that were extracted from a Global Forest Cover (GFC) map [34]. The map provides values of tree cover in percentages, starting from 2000 and updated to 2020, with values from 0% (no forest) to 100% (full tree canopy cover). The map has a resolution of 30 m, as it was produced by classifying Landsat images. The information from [34] also allowed us to map the areas with forest loss due to disturbances. For example, Portugal lost a cumulative of 1.03 million ha from 2001 to 2019 of Mediterranean forests [35]. For this study, the GFC map was used to mask Sentinel-1 images to keep only cells falling inside areas that are covered >90% with tree canopies.

### 2.5. Drought Code Map

Drought Code maps of the study area from 2018 to 2020 were obtained from JRC [36]. They are produced by interpolating DC values from the European Centre for Medium-Range Weather Forecast (ECMWF) network. The pixel resolutions of these maps are approximately  $0.07^\circ$  (~7 km at the average latitude of the study area) for 2019 and 2020, and  $0.14^\circ$  (~14 km at the average latitude of the study area) for 2018. According to [4] and [37], DC is calculated from daily temperature and precipitation records. For rainfall above 2.8 mm, DC is calculated based on rainfall values of the day ( $DC_r$ ) and the DC value of the previous day ( $DC_{t-1}$ ) with the following equations:

$$DC_r = 400 \cdot \ln\left(\frac{800}{Q_r}\right) \quad (1)$$

$$Q_r = Q_{t-1} + 3.937 \cdot r_d \quad (2)$$

$$Q_{t-1} = 800 \cdot \exp\left(\frac{-DC_{t-1}}{400}\right); r_d = 0.83 \cdot r_t - 1.27 \quad (3)$$

where  $DC_r$  is the Drought Code from rainfall data of the day,  $Q_r$  is the moisture equivalent that is calculated from the moisture equivalent of the previous day,  $Q_{t-1}$ , which is in turn calculated from  $DC_{t-1}$ , i.e., the DC code of the last day, and  $r_t$  is the rainfall of the day in mm.

In case of rainfall below 2.8 mm, DC is calculated based on the temperature at mid-day and  $DC_{t-1}$ , i.e., the DC code of the previous day with the following equations:

$$DC_t = DC_{t-1} + 0.5 \cdot V \quad (4)$$

$$V = 0.36 (T_{12} + 2.8) \cdot Lf \quad (5)$$

where  $V$  is the potential evaporation,  $T_{12}$  is the temperature at mid-day, and  $Lf$  is the seasonal day length adjustment.

Because the fire areas are much smaller than the DC map resolution, each DC value results from a bilinear interpolation weighted with distance from the center of the four DC cells. The resulting unitless DC values were classified as extremely low for values less than 256.1 and remarkably high for values greater than 749.4 [38].

### 2.6. Data Processing

Figure 3 presents the methodology used in the study. Dual-polarized images acquired in the satellite's ascending orbit were processed in the Sentinel Application Platform (SNAP) to produce backscatter images— $\sigma^\circ$  in decibels (dB).  $\sigma^\circ$  represents the illuminated target's target backscattering area (radar cross-section). The SNAP platform used the following steps: subsetting, precise orbit file correction, thermal noise removal, radiometric calibration, terrain correction, and conversion to dB. Multi-looking and speckle filtering were skipped to ensure detail preservation and no repetition of the multi-looking process usually done by the Sentinel-1 processing facility. The imagery was orthorectified to the World Geodetic System (WGS) 1984 coordinate system using the Shuttle Radar Topography

Mission (SRTM) 3Sec Digital Elevation Model (DEM). The resulting SAR imagery was subjected to a series of masking as a function of the tree cover and local incidence angles to minimize the effects of these confounding variables.

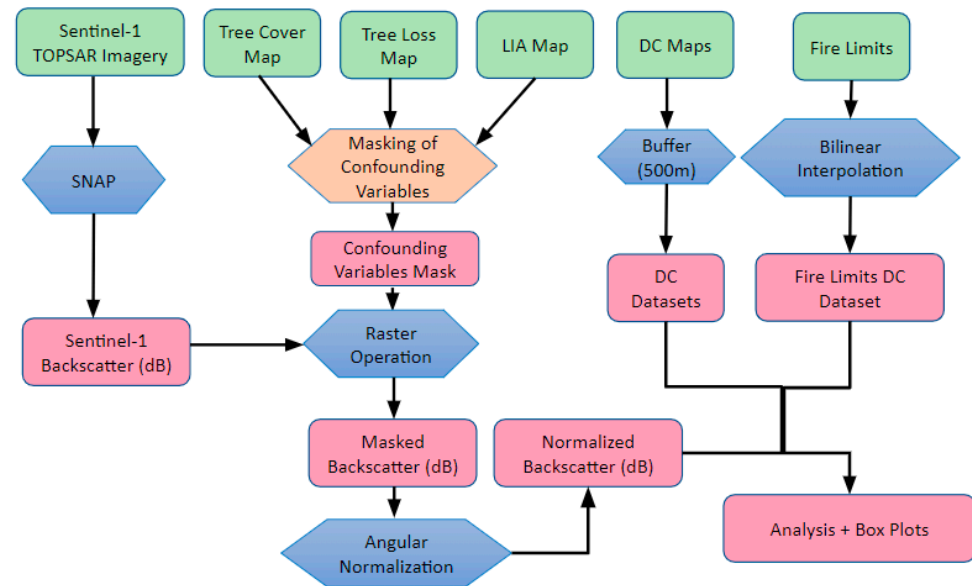


**Figure 3.** Flowchart describing the methodology used in the study.

### 2.6.1. Local Incidence Angle Masking

Local incidence angle (LIA) is defined as the angle of the incident radar beam to the normal of the local surface [39]. SAR backscatter is highly related to LIA [40]. In this study, we only considered areas with a LIA value below  $65^\circ$ . To do so, we created a LIA map using the data from the radar image geometry (look direction angle) and values of slope and aspect angle derived from a digital elevation model (DEM) from the SRTM mission that provides elevation values of the earth's surface [41]. The resulting LIA map was cropped and resampled to match the radar imagery. A LIA mask that keeps only areas with LIA lower than  $65^\circ$  was created. As a result, the LIA value for each scene ranged from  $2.07^\circ$  to  $64.72^\circ$ .

### 2.6.2. Tree Cover Masking

For this research, only burnt (pre-fire periods) and unburnt areas with tree cover higher than 90% were considered, and the other regions were masked out. Such a mask was created from the global scale tree cover of [34], a raster with global tree canopy cover percentage values for each pixel. Values range from zero (no canopy in the pixel) to 100 percent (pixels fully covered with forest canopy).

### 2.6.3. Forest Loss Masking

Forest cover loss occurs through different disturbances, including forest fires. The canopy cover map of Hansen et al., (2013) includes a loss and gain map. The former provides estimated global forest loss information from 2000 to 2020. Values in the map are integers from zero (no loss) to 20, with values above zero representing the loss year since 2000. Forest cover loss information was used to ensure that only areas without a loss (zero value at a pixel) or with loss due to fire were selected for further processing. The pixels with tree cover loss due to a fire event were defined as those with a loss value that spatially and temporally overlapped the fire polygons. These pixels were not masked as they were used in the analysis to assess backscatter behavior changes before and after the fire event.

#### 2.6.4. Cumulative Mask

A final mask was created by simple raster calculation that composited the three masks described above using a multiplication operation. The final mask keeps pixels with forest canopy cover above 90%, canopy loss equal to zero or only with fire loss, and LIA lower than  $65^\circ$ . The resulting pixels were defined as “processed” or “unprocessed” (Figure 4) for reference in the following steps. Backscatter values corresponding to “processed” pixels were further processed, while those corresponding to “unprocessed” pixels were not considered. Backscatter values were further filtered to remove outliers by keeping only backscatter values between  $-0.1$  dB and  $-30$  dB.

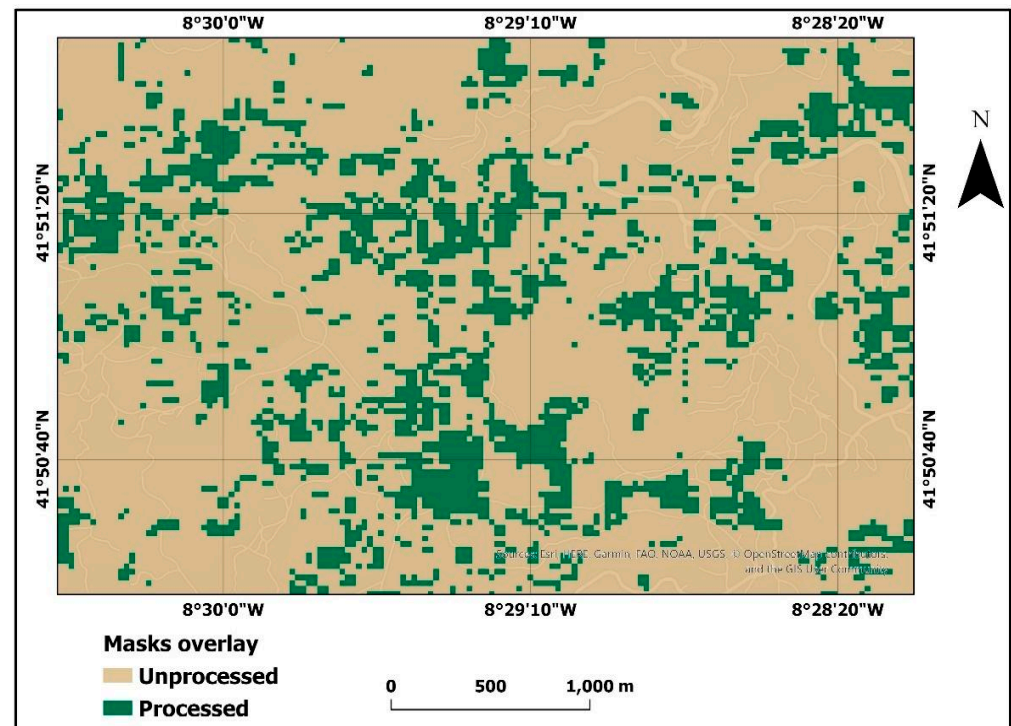


**Figure 4.** Resulting mask obtained by overlaying the masks for tree cover, forest loss, and local incidence angle (LIA). “Processed” pixels are characterized by tree cover higher than 90%, a local incidence angle (LIA) lower than  $65^\circ$ , and a forest loss of 0%.

#### 2.6.5. Backscatter Values Extraction

Given that one of the study objectives is to analyze the connection between radar backscatters and DC values, we used daily DC maps with a resolution of  $0.14^\circ$  in 2018 and  $0.07^\circ$  in 2019 and 2020. The study area corresponds to 60 cell centers for 2018 and 232 for 2019 and 2020. Cell centers of the DC rasters were buffered to a 500 m radius, and all Sentinel-1 pixels falling in the buffer and belonging to the “processed” class (Figure 4) were used to analyze the “Unburnt areas” dataset (Figure 5). Finally, bilinear interpolation was used to assign DC values to SAR pixels in the fire polygons, as these maps are not centered on buffers of DC maps. This last step created the “Burnt Areas Pre-Fire” and “Burnt Areas Post-Fire” datasets.

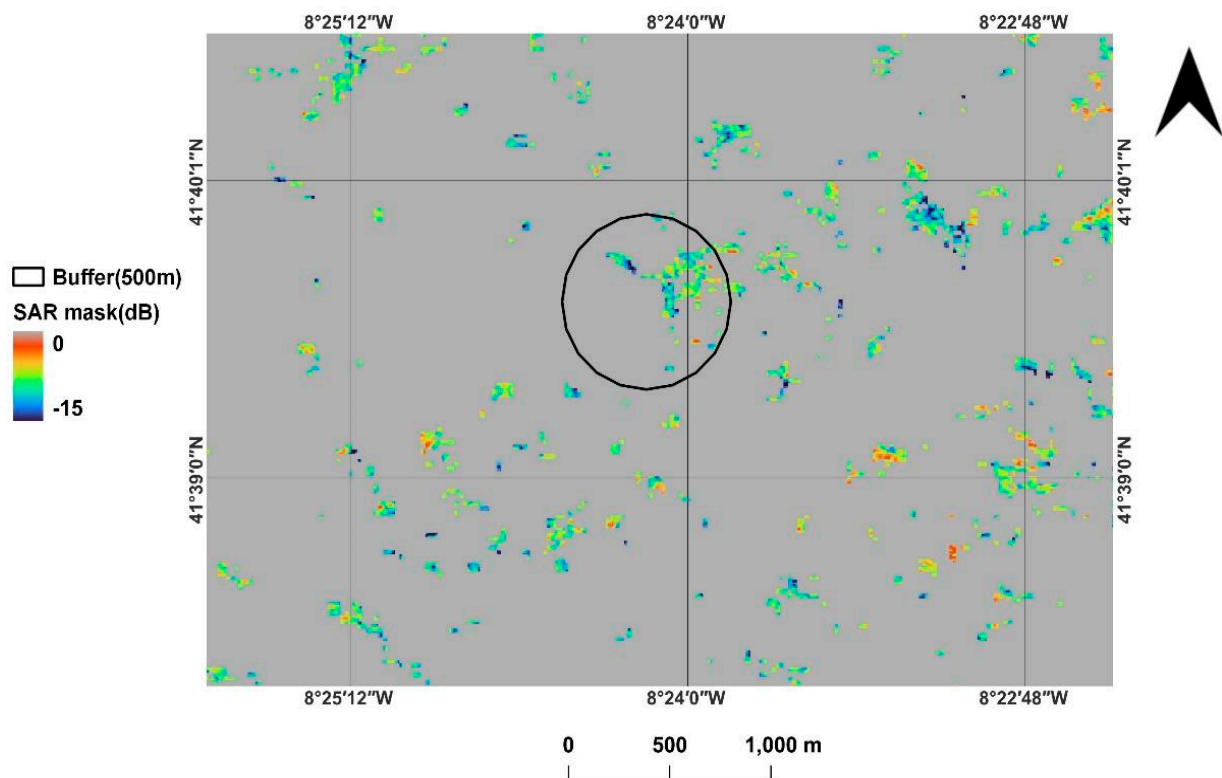


**Figure 5.** 500 m buffer geometry from DC pixel centers overlapping the masked SAR data. SAR backscatter values were correlated to DC values at the time of the image.

### 3. Results

#### 3.1. Unburnt Areas

Our first research question is how DC class affects the backscatter/LIA relation. Figure 6 presents the change of backscatter as a function of LIA values grouped by three factors: (i) the DC class, (ii) the polarization (VV or VH), and (iii) the Sentinel satellite (A or B). The DC values are divided in four classes using a log10-scale (0.1–1, 1–10, 10–100, 100–1000). The log10-scale was used to highlight the DC values of very wet canopy scenarios (0.1–1) from the dry (1–10, 10–100) and very dry (100–1000) scenarios. This choice is because the area has a dry Mediterranean climate. Thus, wet canopy scenarios are less frequent. The DC classes represent a transition between extremely wet and dry soil conditions in unburnt areas. Figure 6 shows that the backscatter decreases with LIA for this study's unburnt and burnt pixels. This result agrees with other studies [18,42].

Following [18], the extracted radar backscatters were normalized for the LIA with the following formula:

$$\underline{\sigma}^{\circ} = \sigma^{\circ} (dB) - \left( \theta_{inc} \times \frac{\Delta\sigma^{\circ}}{\Delta\theta_{inc}} \right) \quad (6)$$

where:

$\underline{\sigma}^{\circ}$  is the corrected backscatter for LIA dependence (dB);

$\sigma^{\circ} (dB)$  is the uncorrected dependent backscatter (dB);

$\theta_{inc}$  is the local incidence angle (LIA) (degree);

$\Delta\sigma^{\circ} / \Delta\theta_{inc}$  is the regression slope provided in Table 1 as a function of the sensor, polarization, and DC class.



**Table 1.** Linear regression between C-VH backscatter values of unburnt pixels and LIA as a function of the sensor, polarization, and DC class. All the regressions have  $p \ll 0.001$ . The colors replicate the color scale in plots of Figure 6.





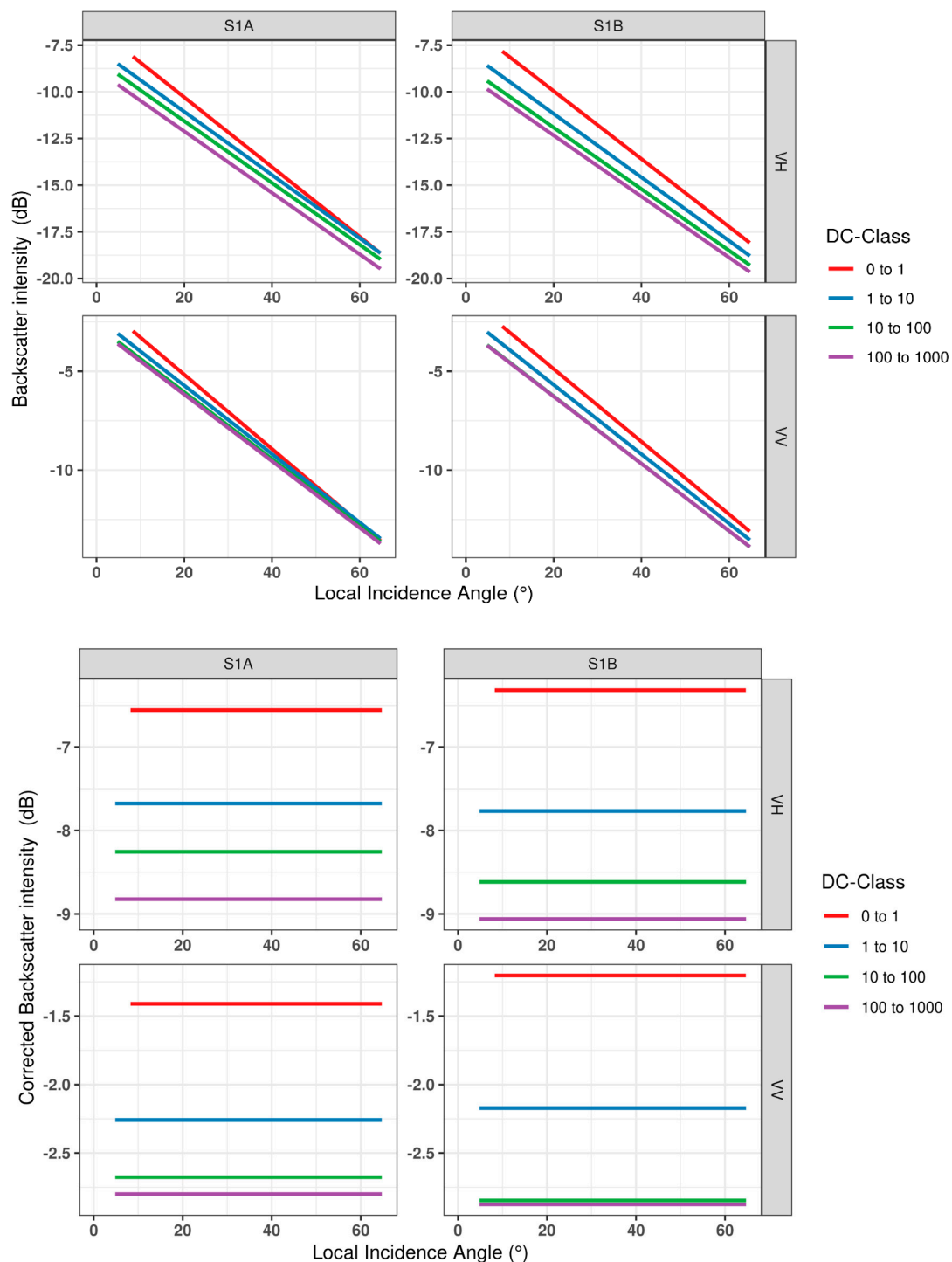
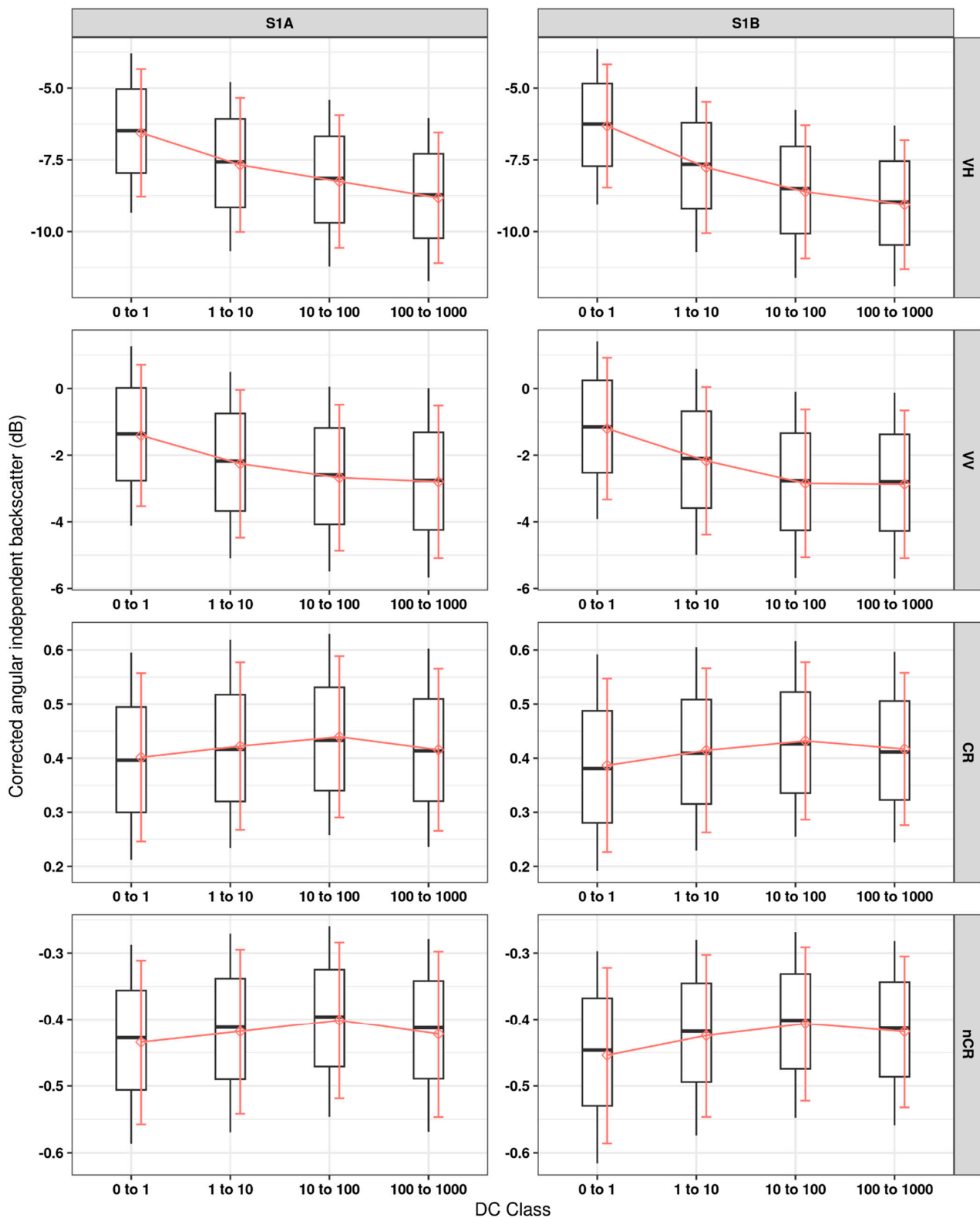
Sensor & Pol.	–	DC-Class	Mean (dB)	Mean DC	Linear Regression Parameters		
					Equation	R <sup>2</sup>	N
S1A VV		0 to 1	−13.61	0.58	$y = -6.20 + -0.19(x)$	0.408	83413
		1 to 10	−13.99	3.94	$y = -7.55 + -0.17(x)$	0.331	735476
		10 to 100	−14.45	35.26	$y = -8.07 + -0.17(x)$	0.328	666649
		100 to 1000	−14.98	346.90	$y = -8.70 + -0.17(x)$	0.324	1143507
S1B VV		0 to 1	−13.24	0.61	$y = -6.14 + -0.19(x)$	0.421	35631
		1 to 10	−14.14	4.48	$y = -7.60 + -0.17(x)$	0.344	703635
		10 to 100	−14.77	35.75	$y = -8.41 + -0.17(x)$	0.326	772728
		100 to 1000	−15.16	343.66	$y = -8.91 + -0.17(x)$	0.329	1114588
S1A VH		0 to 1	−8.51	0.58	$y = -0.94 + -0.20(x)$	0.438	83341
		1 to 10	−8.73	3.92	$y = -2.11 + -0.18(x)$	0.366	739908
		10 to 100	−9.02	35.24	$y = -2.48 + -0.17(x)$	0.365	667006
		100 to 1000	−9.17	342.10	$y = -2.65 + -0.17(x)$	0.356	1117419
S1B VH		0 to 1	−8.17	0.61	$y = -0.99 + -0.19(x)$	0.431	35537
		1 to 10	−8.76	4.49	$y = -1.97 + -0.18(x)$	0.377	702264
		10 to 100	−9.23	35.75	$y = -2.63 + -0.18(x)$	0.364	771789
		100 to 1000	−9.24	343.68	$y = -2.70 + -0.17(x)$	0.359	1113898

Table 1 shows the correlation between LIA and backscatter. We normalized for this correlation in order to remove the confounding effect of LIA with respect to the factor that we are testing, i.e., wet/dry canopy conditions proxied with DC values. It can be noted that, especially on dryer scenarios, the coefficient of determination is lower than 0.4. This is due to the fact that the effect of LIA on backscatter is abated by the structure of the canopy, which has multiple small reflectors (leaves) that are not consistently oriented upwards, and thus the LIA is the integrated value of multi-oriented surfaces. The resulting corrected backscatters do not show any relationship with LIA (Figure 6–bottom). Huang et al. [43] reported the same trend between these two variables but with a different normalization method. Since all the other factors (tree cover and incidence angle) were removed by masking, what is left is the effect of the weather conditions, which is here proxied by the DC values assigned to the backscatter values depending on the day of sensing.



**Figure 6.** Relationship between the LIA and backscatter values (**top**) and corrected backscatter values (**bottom**) in unburnt pixels over canopy cover grouped by DC class.

Figure 7 reports the distribution of backscatter signal intensities aggregated by DC-classes for the two polarizations (VV and VH) and for the cross-ratio (CR)-VH/VV and normalized cross-ratio (nCR)  $(VV-VH)/(VV+VH)$ . It can be seen that VV and VH have a higher sensitivity with respect to CR and nCR, outlining a decreasing trend with increasing DC values (increasing dry conditions.) CR and nCR slightly increase and then decrease at the higher DC values.



**Figure 7.** Distribution of corrected backscatter values in unburnt pixels with the DC classes for the two polarizations (VV and VH) and for the cross-ratio (CR)-VH/VV and normalized cross-ratio (nCR)  $(VV-VH)/(VV+VH)$ . Red lines connect the average values, red whiskers are standard deviation, boxplots are the medians and interquartile ranges, with whiskers corresponding to the 10th and 90th percentile.

Table 2 shows the statistical significance of the differences of medians, which is quite high, due to the very high number of samples (pixels) used in the test. It must be noted that this gives us confidence with respect to the results, but the variance is not negligible.

**Table 2.** Pairwise differences between DC classes: A = 0 to 1, B = 1 to 10, C = 10 to 100, D = 100 to 1000. Adjusted  $p$ -Value  $\ll 0.001$ .

Polarization	Sensor	DC Class Pair	Mean Backscatter Difference.	Lower end Confidence Interval	Upper end Confidence Interval
VV	S1A	B-A	−0.85	−0.92	−0.78
		C-B	−0.42	−0.45	−0.39
		D-C	−0.12	−0.15	−0.09
	S1B	B-A	−0.97	−1.07	−0.86
		C-B	−0.67	−0.70	−0.64
		D-C	−0.03	−0.06	0.00
VH	S1A	B-A	−1.12	−1.19	−1.04
		C-B	−0.58	−0.61	−0.55
		D-C	−0.57	−0.60	−0.54
	S1B	B-A	−1.45	−1.56	−1.34
		C-B	−0.85	−0.88	−0.82
		D-C	−0.44	−0.47	−0.42

### 3.2. Burnt Areas

The second research question relates to the fire effect on the relationship between corrected backscatter and DC classes. Results in this section represent observations over pre-fire and post-fire periods. For the post-fire data, the C-VV polarization was not considered because the C-VH polarization clearly provided better discrimination of DC classes than the C-VV polarization (see Figures 6 and 7). To better understand the post-fire behavior of radar backscatters, the post-fire period was divided into classes of the number of days after the fire (0 to 30, 30 to 90, 90 to 180, 180 to 360, and 360 to inf.). Boxplots corresponding to DC class (0 to 10) are missing for the 0 to 30 and 30 to 90 periods after fire for the S1-B case because of a lack of imagery. Results before the fire are very similar to un-burned areas but are quite different after the fire.

Figures 8 and 9 represent the situation on fire areas, before and after the fire. As noted, the pre-fire situation is very similar to the results seen in un-burned areas, even if less marked. Post-fire situation is very different, especially in the first months after the fire. This is further discussed in the next section.

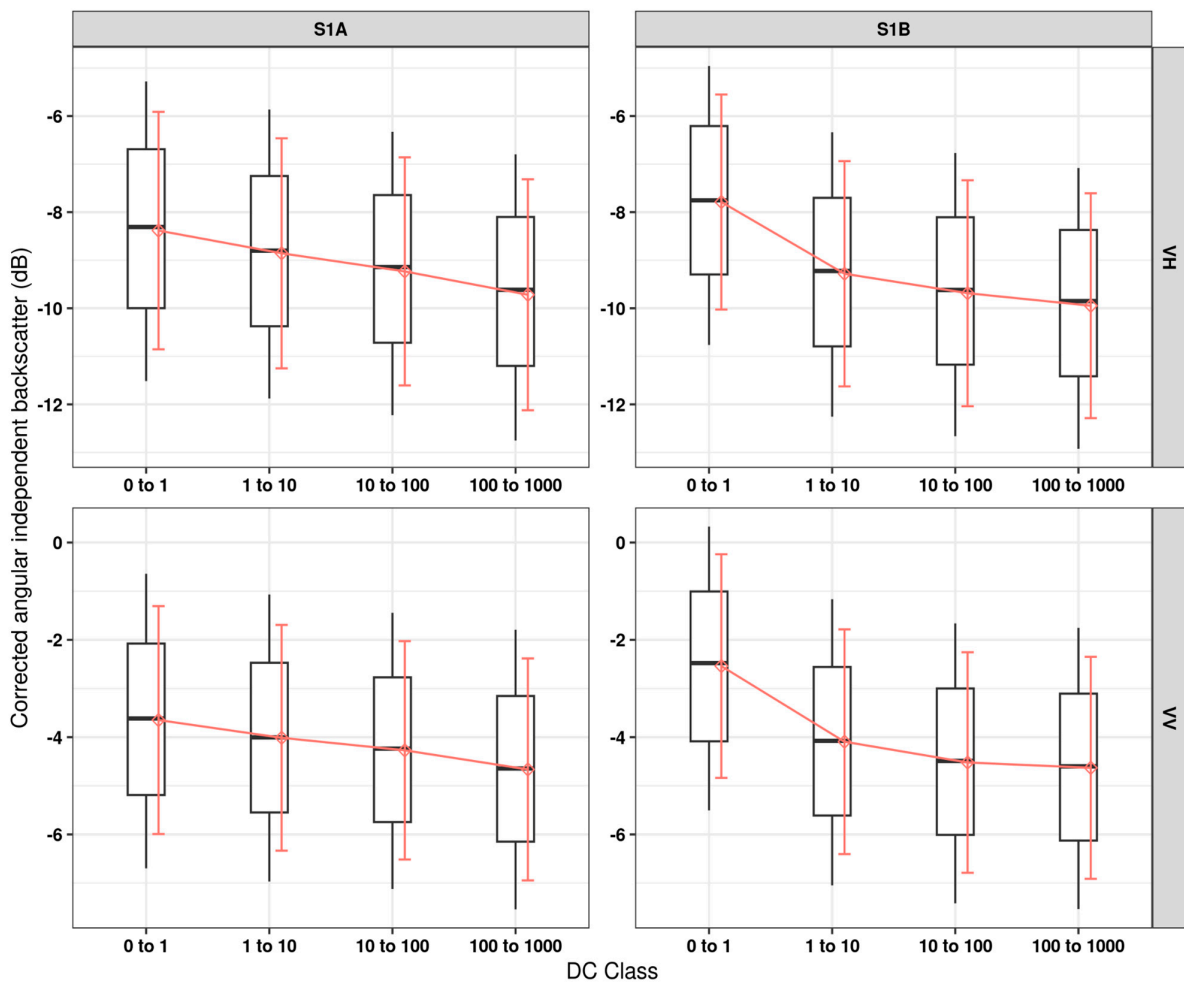


**Figure 8.** Distribution of corrected backscatter values before fire in fire-affected pixels with the DC classes. Red lines connect the average values, red whiskers are standard deviation, boxplots are the medians and interquartile ranges, with whiskers corresponding to the 10th and 90th percentile.

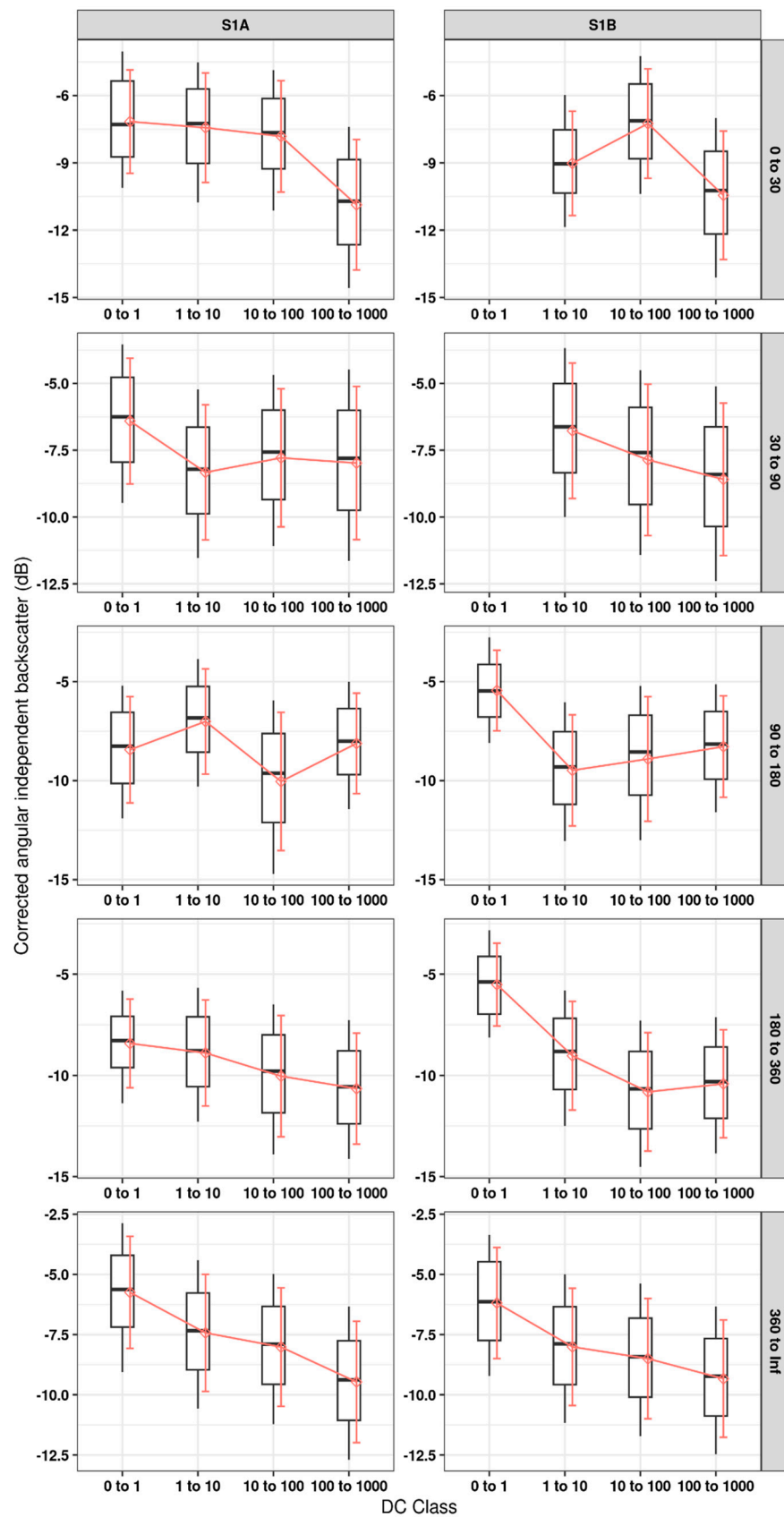


Figure 9. Distribution of corrected Sentinel-1 C-VH backscatter, grouped by DC class with rows representing the days from the fire event and columns the two Sentinel-1 sensors A and B.

#### 4. Discussion

The response to canopy moisture of Sentinel-1 backscatter values over unburnt forest areas in Figure 7 clearly showed an inverse correlation, as it decreased on DC classes with higher values. This was more clearly visible over very low DC values, where results showed that the backscatter intensity tends to be stronger when reflected by wet canopies (DC class = 0.1 to 1). This is less clearly seen, even if still compatible with a decreasing trend, in less wet (DC class = 1 to 10, 10 to 100) and extremely dry (DC class = 100 to 1000) soils. C-VH polarization shows better discrimination of canopy moisture conditions with respect to C-VV. The S1-B has a lower effect than the S1-A in terms of mean backscatter values. The DC index was created to represent the wetness of the slow-drying deep layers of the soil. DC values above 1 mean that the soils in that situation are drying up, and lower values indicate that they are wet. DC values corresponding to dry conditions were only observed in July, August, September, and October 2018.

For the unburnt areas, boxplots in Figure 8 shows that the backscatter average is significantly different between all pairwise comparisons between DC classes (Table 2). It is worth noting also that C-VH is more sensible with respect to C-VV, as can be noted in Table 2. The C-VH backscatter difference between the lower DC class (0 to 1) and the next class (1 to 10) was 1.12 dB and 1.45 dB, respectively, for A and B sensors of Sentinel-1, compared to 0.85 dB and 0.97 dB in C-VV (Table 2). This result is compatible with the work [44] carried out over a Savannah ecosystem. The higher sensitivity of C-VH to the DC values is likely linked to the fact that the relative scattering strength of C-VH is mainly volume scattering, i.e., vegetation canopy ([45]—Table 1). Moreover, in VH biomass backscattering, contributions from the surface and double-bounce scatterers are minimal [46], and therefore high accuracy of volume scattering is expected in the pre-burn datasets. Co-polarized C-VV scattering strength is mainly double bounce and rough surface scattering [45,46]. This is also seen in [47], where dry conditions result in 1 to 2 dB lower backscatter in crops with drought conditions with respect to normal conditions. Our work is on a different scenario, forest canopy, but provides comparable results, adding that such a difference can be seen also over a small change of wet to dry conditions, without having to compare very wet conditions to drought conditions. With respect to [47], it is also worth noting that the cross-ratio (CR, VH/VV) was tested (see Figure 7), but, differently from the other work, it did not provide significant results as much as the single VV and VH polarizations did.

The analysis over the burnt areas shows that in the pre-fire observations, the relationship between normalized backscattered intensity and DC classes is similar to that of the unburnt areas (Figure 8), as would be expected. However, with respect to observations over unburnt areas in Figure 7, the mean backscatter values in Figure 8 are less sensitive to different DC scenarios. A reasonable explanation could be that the DC values in areas that had a fire event were interpolated from the nearest four DC values. It must be noted that DC values are created by interpolation of weather data and thus we can expect that the DC value assigned to backscatter values recorded in the burnt areas is not as accurate as the one assigned to the unburnt areas. It should be noted that DC values are interpolated by a model and thus carry uncertainty. Undoubtedly DC values calculated with dedicated climate sensors positioned at each cell node and at each burnt area would increase reliability with respect to interpolated values, and also the results would benefit from higher quality observed DC values, but this is an ideal scenario that was not available.

Figure 9 shows that in post-fire scenarios, the C-VH backscatter values lose the correlation with DC classes that were observed over the unburned sites (Figure 7) and over the burnt sites before the fire (Figure 8). This holds true for the period right after the fire to ~360 days. After that date, the backscatter values behave, with respect to DC classes, the same as the unburnt and pre-fire scenarios. One plausible explanation for this result is the different dielectric properties of burnt branches and leaves that change the backscatter values, as highlighted in [18]. After one year, i.e., 360 days, the backscatter-DC relation returned to the one observed before the fire (Figure 8). A reasonable hypothesis for the loss of the inverse correlation between C-VH and DC values right after a fire up to 360 days is

the decrease of the volume scattering component, i.e., the leaves in the canopy crown. After a fire event, the leaves are charred if not completely burned, thus not contributing to the volume scattering as much as healthy leaves [48,49]. As explained in [50], diverging trends in C-band post-fire backscattering can also be attributed to vegetation death changing the structure of the canopy, leaving dry branches and a minimum number of dead leaves.

After 360 days from the fire event, the C-VH captured vegetation recovery but was less sensitive in terms of distinction of extremely dry sites, as seen in pre-fire and unburnt observations. For instance, for the S1-B cases, the average corrected backscatter corresponding to the 360 to Inf period (Figure 9) was  $-7.5$  dB, compared to  $-5$  dB for the pre-fire observations in Figure 8. As already shown by [51], C-band backscatters used for monitoring post-fire vegetation recovery are influenced by several factors. In particular, post-fire C-band backscatters never returned to the pre-fire levels due to the disturbance of the vegetation structure and density from the fire. Since the C-VH is sensitive to vegetation structure, the C-VH backscatter also depends on the post-fire regeneration rate. By contrast, [52] reported that the L-band performed better than the C-band in change detection of post-fire vegetation structure in a Mediterranean environment. Therefore, it is preferable to use a combination of L and C bands [52,53]. An even better method is the synergistic use of radar and optical images, given that they give different information over the surveyed area [54–56].

## 5. Conclusions

Time series of 10 m Sentinel-1 C-VV and C-VH data, acquired from January 2018 to December 2020, were used to analyze the correlation between backscatter and canopy wetness derived from using DC values as proxy. The study was carried out over  $502.42$  km<sup>2</sup> in north-western Portugal. C-VH radar backscatters were found to be better related to the DC values than C-VV radar backscatters. Low DC values, i.e., less than or equal to 1, have a median C-VH backscatter about 2 dB higher with respect to DC values above 10. As observed in the unburnt sites, the relationship between backscatter and DC was monitored in the sites affected by fire events over the three years of satellite coverage. Results show that right after a fire event the C-VH backscatter response is not correlated to canopy wetness and that an average of 360 or more days from the fire date are necessary for canopies to recover such response to pre-fire situations.

The study was done in a Mediterranean region of north-western Portugal with specific tree species, and it is necessary to have this analysis conducted over other Mediterranean regions with other tree species. In addition, bilinear interpolation was used to assign DC values to the fire maps, as the sourced FWI-related weather records have low spatial resolutions. Therefore, high-resolution DC data should ensure that spatially derived DC values represent fine-scale soil moisture conditions.

The relationship between DC and backscatter of C-band VH polarization can help to map moisture conditions across forest covers. This is an important asset that will be further investigated. It must be noted though that the model is applicable to the same conditions used in our data; therefore, a forest cover equal to or greater than 90%. Furthermore, the post-fire sensitivity of radar backscatters to DC can highlight fuel readiness for another fire ignition. As shown in Figure 9, the relationship between radar backscatters and DC, after a recovery period of 360 days, behaved similarly to the pre-fire scenarios. As such, it can be inferred that fire events have occurred after this recovery period.

Future work can include validation of the potential prediction power of VH backscatter for defining a map of DC values, comparing it with values from official DC maps and calculated from climate sensors. This validation process was not included in this work as we focus on results regarding how backscatter changes with DC scenarios.



**Author Contributions:** Conceptualization, F.P.; methodology, B.L. and F.P.; writing—original draft preparation, O.A., B.L. and F.P.; writing—review and editing, O.A., B.L. and F.P.; supervision, B.L. and F.P. All authors have read and agreed to the published version of the manuscript.

**Funding:** This study was carried out within the funding of the National Research Center for Agricultural Technologies (AGRITECH) from the European Union Next-GenerationEU Piano Nazionale di Ripresa e Resilienza (PNRR)–M4C2 Investimento 1.4–D.D. 1032 17/06/2022, CN00000022–CUP HUB B63D21015240004. This manuscript reflects only the authors’ views and opinions; neither the European Union nor the European Commission can be considered responsible for them.

**Data Availability Statement:** Publicly available datasets were analyzed in this study. Sentinel-1 data are available via the Copernicus Open Science Hub (<https://scihub.copernicus.eu/>), drought code maps are available upon request to the EU Joint Research Center <https://effis.jrc.ec.europa.eu/apps/data.request.form/>. Processed data and methods used in this study are openly available as R scripts and data in <https://zenodo.org/record/7419555>.

**Acknowledgments:** The authors wish to acknowledge EU Joint Research Center for providing spatially derived DC datasets.

**Conflicts of Interest:** The authors declare no conflict of interest.

## References

- Pinto, M.M.; DaCamara, C.C.; Trigo, I.F.; Trigo, R.M.; Turkman, K.F. Fire danger rating over Mediterranean Europe based on fire radiative power derived from Meteosat. *Nat. Hazards Earth Syst. Sci.* **2018**, *18*, 515–529. [CrossRef]
- Pyne, S.J. *Eternal Flame: An Introduction to the Fire History of the Mediterranean*. In *Earth Observation of Wildland Fires in Mediterranean Ecosystems*; Springer: Berlin/Heidelberg, Germany, 2009; pp. 11–26.
- Gonçalves, A.C.; Sousa, A.M.O. *The Fire in the Mediterranean Region: A Case Study of Forest Fires in Portugal. Mediterranean Identities—Environment, Society, Culture*; InTech: London, UK, 2017; p. 311.
- Van Wagner, C. *Development and Structure of the Canadian Forest Fire Weather Index System*; Forestry Technical Report, N°35; Canadian Forestry Service: Petawawa, ON, Canada, 1987; p. 13.
- Wotton, B.M. Interpreting and using outputs from the Canadian Forest Fire Danger Rating System in research applications. *Environ. Ecol. Stat.* **2009**, *2*, 107–131. [CrossRef]
- Leblon, B.; Kasischke, E.; Alexander, M.; Doyle, M.; Abbott, M. Fire Danger Monitoring Using ERS-1 SAR Images in the Case of Northern Boreal Forests. *Nat. Hazards* **2002**, *27*, 231–255. [CrossRef]
- Yang, G.; Di, X. Adaptation of Canadian Forest Fire Weather Index System and Its Application. In Proceedings of the IEEE International Conference on Computer Science and Automation Engineering, Shanghai, China, 10–12 June 2011; pp. 55–58.
- Dimitrakopoulos, A.P.; Bemmerzouk, A.M.; Mitsopoulos, I.D. Evaluation of the Canadian fire weather index system in an eastern Mediterranean environment. *Meteorol. Appl.* **2011**, *18*, 83–93. [CrossRef]
- Oldford, S.; Leblon, B.; Maclean, D.; Flannigan, M. Predicting slow-drying fire weather index fuel moisture codes with NOAA-AVHRR images in Canada’s northern boreal forests. *Int. J. Remote Sens.* **2006**, *27*, 3881–3902. [CrossRef]
- Available online: <https://www.ecmwf.int/sites/default/files/elibrary/2012/17412-describing-ecmwfs-forecasts-and-forecasting-system.pdf> (accessed on 22 January 2022).
- Leblon, B. Monitoring Forest Fire Danger with Remote Sensing. *Nat. Hazards* **2005**, *35*, 343–359. [CrossRef]
- Rostami, A.; Shah-Hosseini, R.; Asgari, S.; Zarei, A.; Aghdami-Nia, M.; Homayouni, S. Active Fire Detection from Landsat-8 Imagery Using Deep Multiple Kernel Learning. *Remote Sens.* **2002**, *14*, 992. [CrossRef]
- Available online: <https://cwfis.cfs.nrcan.gc.ca/background/summary/fwi> (accessed on 22 January 2022).
- Vetrita, Y.; Prasasti, I.; Haryani, N.S.; Priyatna, M.; Rokhis Khomarudin, M. Drought and Fine Fuel Moisture Code Evaluation: An Early Warning System for Forest/Land Fire using Remote Sensing Approach. *Int. J. Remote Sens.* **2012**, *9*, 140–147. [CrossRef]
- Lee, J.-S.; Pottier, E. *Polarimetric Radar Imaging: From Basics to Applications (Optical Science and Engineering)*; CRC Press: Boca Raton, FL, USA, 2009; pp. 5–6.
- Ruiz-Ramos, J.; Marino, A.; Boardman, C.P. Using Sentinel 1-SAR for monitoring long-term variation in burnt forest areas. In Proceedings of the International Geoscience and Remote Sensing Symposium (IGARSS), Valencia, Spain, 22–27 July 2018; pp. 4901–4904.
- Bourgeau-Chavez, L.L.; Leblon, B.; Charbonneau, F.; Buckley, J.R. Assessment of polarimetric SAR data for discrimination between wet versus dry soil moisture conditions. *Int. J. Remote Sens.* **2013**, *34*, 5709–5730. [CrossRef]
- Abbott, K.N.; Leblon, B.; Staples, G.C.; Maclean, D.A.; Alexander, M.E. Fire danger monitoring using RADARSAT-1 over northern boreal forests. *Int. J. Remote Sens.* **2007**, *28*, 1317–1338. [CrossRef]
- Bourgeau-Chavez, L.L.; Riordan, K.; Garwood, G. Monitoring Fuel Moisture and Improving the Prediction of Wildfire Potential in Boreal Alaska with Satellite C-Band Imaging Radar. In Proceedings of the IEEE International Geoscience and Remote Sensing Symposium, Boston, MA, USA, 8–11 July 2008; pp. 864–866.

20. Leblon, B.; Bourgeau-Chavez, L.; San-Miguel-Ayanz, J. Use of Remote Sensing in Wildfire Management. In *Sustainable Development—Authoritative and Leading Edge Content for Environmental Management*, 1st ed.; Curkovic, S., Ed.; IntechOpen: London, UK, 2012; Chapter 3; p. 63.
21. Torres, R.; Snoeij, P.; Geudtner, D.; Bibby, D.; Davidson, M.; Attema, E.; Potin, P.; Rommen, B.; Floury, N.; Brown, M.; et al. GMES Sentinel-1 mission. *Remote Sens. Environ.* **2012**, *120*, 9–24. [[CrossRef](#)]
22. Soudani, K.; Delpierre, N.; Berveiller, D.; Hmimina, G.; Vincent, G.; Morfin, A.; Dufrière, É. Potential of C-band Synthetic Aperture Radar Sentinel-1 time-series for the monitoring of phenological cycles in a deciduous forest. *Int. J. Appl. Earth Obs. Geoinf.* **2021**, *12*, 102505. [[CrossRef](#)]
23. Sutariya, S.; Hirapara, A.; Meherbanali, M.; Tiwari, M.K.; Singh, V.; Kalubarme, M. Soil Moisture Estimation using Sentinel-1 SAR Data and Land Surface Temperature in Panchmahal District, Gujarat State. *Int. J. Environ. Geoinformatics* **2021**, *8*, 65–77. [[CrossRef](#)]
24. Wang, L.; Quan, X.; He, B.; Yebra, M.; Xing, M.; Liu, X. Assessment of the Dual Polarimetric Sentinel-1A Data for Forest Fuel Moisture Content Estimation. *Remote Sens.* **2019**, *11*, 1568. [[CrossRef](#)]
25. Available online: [http://ecofun.fc.ul.pt/Activities/Desertification2014/docs2/SousaUva\\_The%20Portuguese%20National%20Forest%20Inventory.pdf](http://ecofun.fc.ul.pt/Activities/Desertification2014/docs2/SousaUva_The%20Portuguese%20National%20Forest%20Inventory.pdf) (accessed on 14 January 2022).
26. Kotteck, M.; Grieser, J.; Beck, C.; Rudolf, B.; Rubel, F. World Map of the Köppen-Geiger climate classification updated. *Meteorol. Z.* **2006**, *15*, 259–263. [[CrossRef](#)] [[PubMed](#)]
27. Available online: <https://www.ipma.pt/pt/oclima/normais.clima/1981-2010/normalclimate8110.jsp> (accessed on 14 January 2014).
28. Pereira, M.G.; Trigo, R.M.; da Camara, C.C.; Pereira, J.M.C.; Leite, S.M. Synoptic patterns associated with large summer forest fires in Portugal. *Agric. For. Meteorol.* **2005**, *129*, 11–25. [[CrossRef](#)]
29. San-Miguel-Ayanz, J.; Durrant, T.; Boca, R.; Maianti, P.; Libertá, G.; Artes Vivancos, T.; Jacome Felix Oom, D.; Branco, A.; De Rigo, D.; Ferrari, D.; et al. *Forest Fires in Europe, Middle East and North Africa 2020*; Publications Office of the European Union: Luxembourg, 2021; p. 70.
30. Paulo, B.; Giuseppe, A.; Roberto, B.; Andrea, C.; Jan, K.; Giorgio, L.; San-Miguel-Ayanz, J.; Guido, S.; Ernst, S.; Hans-Helmut, D. *Forest Fires in Europe 2006*; Publications Office of the European Union: Luxembourg, 2007; p. 25.
31. Schubert, A.; Miranda, N.; Geudtner, D.; Small, D. Sentinel-1A/B Combined Product Geolocation Accuracy. *Remote Sens.* **2017**, *9*, 607. [[CrossRef](#)]
32. San-Miguel-Ayanz, J.; Durrant, T.; Boca, R.; Maianti, P.; Libertá, G.; Artés-Vivancos, T.; Oom, D.; Branco, A.; de Rigo, D.; Ferrari, D.; et al. *Advance Report on Forest Fires in Europe, Middle East and North Africa 2021*; Publications Office of the European Union: Luxembourg, 2022; p. 4.
33. Enes, T.; Lousada, J.; Aranha, J.; Cerveira, A.; Alegria, C.; Fonseca, T. Size-density trajectory in regenerated maritime pine stands after fire. *Forests* **2019**, *10*, 1057. [[CrossRef](#)]
34. Hansen, M.C.; Potapov, P.V.; Moore, R.; Hancher, M.; Turubanova, S.A.; Tyukavina, A.; Thau, D.; Stehman, S.V.; Goetz, S.J.; Loveland, T.R.; et al. High-Resolution Global Maps of 21st-Century Tree cover Change. *J. Sci.* **2013**, *342*, 850–853.
35. Ciobotaru, A.M.; Patel, N.; Pintilii, R.D. Tree cover loss in the Mediterranean region—An increasingly serious environmental issue. *Forests* **2021**, *12*, 1341. [[CrossRef](#)]
36. Di Giuseppe, F.; Vitolo, C.; Krzeminski, C.; Barnard, C.; Maciel, C.; San-Miguel-Ayanz, J. Fire Weather Index: The skill provided by the European Centre for Medium-Range Weather Forecasts ensemble prediction. *Nat. Hazards Earth Syst. Sci.* **2020**, *20*, 2365–2378. [[CrossRef](#)]
37. Turner, J.A. *The Drought Code Component of the Canadian Forest Fire Behaviour System*; Canadian Forestry Service Headquarters: Ottawa, ON, Canada, 1972; p. 5.
38. Available online: <https://effis.jrc.ec.europa.eu/about-effis/technical-background/fire-danger-forecast> (accessed on 14 February 2022).
39. Kaplan, G.; Fine, L.; Lukyanov, V.; Manivasagam, V.S.; Tanny, J.; Rozenstein, O. Normalizing the local incidence angle in sentinel-1 imagery to improve leaf area index, vegetation height, and crop coefficient estimations. *Land* **2021**, *10*, 680. [[CrossRef](#)]
40. O’Grady, D.; Leblanc, M.; Gillieson, D. Relationship of local incidence angle with satellite radar backscatter for different surface conditions. *Int. J. Appl. Earth Obs. Geoinf.* **2013**, *24*, 42–53. [[CrossRef](#)]
41. Vollrath, A.; Mullissa, A.; Reiche, J. Angular-based radiometric slope correction for Sentinel-1 on Google Earth Engine. *Remote Sens.* **2020**, *12*, 1867. [[CrossRef](#)]
42. Paluba, D.; Laštovička, J.; Mouratidis, A.; Štych, P. Land cover-specific local incidence angle correction: A method for time-series analysis of forest ecosystems. *Remote Sens.* **2021**, *13*, 1743. [[CrossRef](#)]
43. Huang, W.; Sun, G.; Ni, W.; Zhang, Z.; Dubayah, R. Sensitivity of multi-source SAR backscatter to changes in forest aboveground biomass. *Remote Sens.* **2015**, *7*, 9587–9609. [[CrossRef](#)]
44. Mathieu, R.; Main, R.; Roy, D.P.; Naidoo, L.; Yang, H. The Effect of Surface Fire in Savannah Systems in the Kruger National Park (KNP), South Africa, on the Backscatter of C-Band Sentinel-1 Images. *Fire* **2019**, *2*, 37. [[CrossRef](#)]
45. Kellndorfer, J. Using SAR Data for Mapping Deforestation and Forest Degradation. In *The SAR Handbook: Comprehensive Methodologies for Forest Monitoring and Biomass Estimation*; Flores-Anderson, A.I., Herndon, K.E., Thapa, R.B., Cherrington, E., Eds.; NASA: Huntsville, AL, USA, 2019; p. 68.

46. Meyer, F. Spaceborne Synthetic Aperture Radar: Principles, Data Access, and Basic Processing Techniques. In *The SAR Handbook: Comprehensive Methodologies for Forest Monitoring and Biomass Estimation*; Flores-Anderson, A.I., Herndon, K.E., Thapa, R.B., Cherrington, E., Eds.; NASA: Huntsville, AL, USA, 2019; p. 28.
47. Shorachi, M.; Kumar, V.; Steele-Dunne, S.C. Sentinel-1 SAR Backscatter Response to Agricultural Drought in The Netherlands. *Remote Sens.* **2022**, *14*, 2435. [[CrossRef](#)]
48. Imperatore, P.; Azar, R.; Calo, F.; Stroppiana, D.; Brivio, P.A.; Lanari, R.; Pepe, A. Effect of the Vegetation Fire on Backscattering: An Investigation Based on Sentinel-1 Observations. *IEEE J. Sel. Top. Appl.* **2017**, *10*, 4478–4492. [[CrossRef](#)]
49. Tanase, M.A.; Santoro, M.; de La Riva, J.; Pérez-Cabello, F.; le Toan, T. Sensitivity of X-, C-, and L-Band SAR Backscatter to Burn Severity in Mediterranean Pine Forests. *IEEE Trans. Geosci. Remote Sens.* **2010**, *48*, 3663. [[CrossRef](#)]
50. Belenguer-Plomer, M.; Chuvieco, E.; Tanase, M. Temporal Decorrelation of C-Band Backscatter Coefficient in Mediterranean Burned Areas. *Remote Sens.* **2019**, *11*, 2661. [[CrossRef](#)]
51. Zhou, Z.; Liu, L.; Jiang, L.; Feng, W.; Samsonov, S.V. Using long-term SAR backscatter data to monitor post-fire vegetation recovery in tundra environment. *Remote Sens.* **2019**, *11*, 2230. [[CrossRef](#)]
52. Tanase, M.; de la Riva, J.; Santoro, M.; Pérez-Cabello, F.; Kasischke, E. Sensitivity of SAR data to post-fire forest regrowth in Mediterranean and boreal forests. *Remote Sens. Environ.* **2011**, *115*, 2075–2085. [[CrossRef](#)]
53. Tanase, M.A.; Santoro, M.; Aponte, C.; de la Riva, J. Polarimetric Properties of Burned Forest Areas at C- and L-Band. *IEEE J. Sel. Top. Appl.* **2014**, *7*, 267–276. [[CrossRef](#)]
54. Bernhard, E.-M.; Stein, E.; Twele, A.; Gähler, M. Synergistic use of optical and radar data for rapid mapping of forest fires in the European Mediterranean. *ISPRS Archives.* **2012**, *4*, 27–32. [[CrossRef](#)]
55. LaRocque, A.; Phiri, C.; Leblon, B.; Pirotti, F.; Connor, K.; Hanson, A. Wetland Mapping with Landsat 8 OLI, Sentinel-1, ALOS-1 PALSAR, and LiDAR Data in Southern New Brunswick, Canada. *Remote Sens.* **2020**, *12*, 2095. [[CrossRef](#)]
56. Vaglio Laurin, G.; Puletti, N.; Tattoni, C.; Ferrara, C.; Pirotti, F. Estimated Biomass Loss Caused by the Vaia Windthrow in Northern Italy: Evaluation of Active and Passive Remote Sensing Options. *Remote Sens.* **2021**, *13*, 4924. [[CrossRef](#)]

**Disclaimer/Publisher’s Note:** The statements, opinions and data contained in all publications are solely those of the individual author(s) and contributor(s) and not of MDPI and/or the editor(s). MDPI and/or the editor(s) disclaim responsibility for any injury to people or property resulting from any ideas, methods, instructions or products referred to in the content.